A&A 669, A93 (2023)
https://doi.org/10.1051/0004-6361/202244618

Astronomy & Astrophysics

Laboratory spectroscopy of allylimine and tentative detection towards the G+0.693-0.027 molecular cloud

D. Alberton[1], L. Bizzocchi[2], N. Jiang[2], M. Melosso[2,3], V. M. Rivilla[4], A. Pietropolli Charmet[5], B.M. Giuliano[1], P. Caselli[1], C. Puzzarini[2], S. Alessandrini[2,6], L. Dore[2], I. Jiménez-Serra[4], and J. Martín-Pintado[4]

[1] Center for Astrochemical Studies, Max-Planck-Institut für extraterrestrische Physik, Gießenbachstr. 1, 85748 Garching, Germany
e-mail: alberton@mpe.mpg.de
[2] Dipartimento di Chimica "Giacomo Ciamician", Università di Bologna, via F. Selmi 2, 40126 Bologna, Italy
[3] Scuola Superiore Meridionale, Largo San Marcellino 10, 80136 Naples, Italy
[4] Centro de Astrobiología (CSIC-INTA), Ctra. de Ajalvir Km. 4, Torrejón de Ardoz, 28850 Madrid, Spain
[5] Dipartimento di Scienze Molecolari e Nanosistemi, Università Ca' Foscari Venezia, Via Torino 155, 30172 Mestre, Italy
[6] Scuola Normale Superiore, Piazza dei Cavalieri 7, 56126 Pisa, Italy

Received 28 July 2022 / Accepted 13 October 2022

ABSTRACT

Context. Substituted methanimines and ethylenes have been identified in the interstellar medium. Therefore, allylimine (CH_2=CH−CH=NH) represents a promising candidate for a new interstellar detection.
Aims. The goal of the present work is to perform a comprehensive laboratory investigation of the rotational spectrum of allylimine in its ground vibrational state in order to obtain a highly precise set of rest frequencies to assist its search for astronomical sources.
Methods. The rotational spectra of the two most stable trans–anti and trans–syn geometrical isomers of allylimine were recorded in the laboratory in the 84–300 GHz frequency interval. Measurements were performed using a source-modulation millimetre-wave spectrometer equipped with a pyrolysis system for the production of unstable species. High-level ab initio calculations were performed to assist the analysis and to obtain reliable estimates for an extended set of spectroscopic parameters. Guided by new laboratory data, allylimine was searched for in space using a sensitive spectral survey of the G+0.693-0.027 molecular cloud, located at the Galactic centre.
Results. Almost 1000 rotational transitions have been recorded for trans–anti and trans–syn allylimine. These new data have enabled the determination of a very accurate set of spectroscopic parameters including rotational, quartic and sextic centrifugal distortion constants, as well as nuclear quadrupole coupling constants. The improved spectral data allowed us to report a tentative detection for both allylimine isomers in the G+0.693-0.027 molecular cloud, located at the Galactic centre.

Key words. ISM:molecules – techniques: spectroscopic – line: identification – astrochemistry – methods: laboratory: molecular – ISM: abundances

1. Introduction

To date, about 280 molecules have been detected in the interstellar medium (ISM) in a wide variety of environments, spanning from molecular clouds to late-type stars (see e.g., Endres et al. 2016)[1]. In recent years, the number of comparatively large species increased, and complex organic molecules (COMs, Herbst & van Dishoeck 2009) have generated a substantial amount of interest because their presence in the ISM suggests that chemical complexity starts already in the earliest stages of star formation. Furthermore, the discovery of many amino acids in carbonaceous chondrites (Snyder et al. 2005; Aponte et al. 2020) and the identification of glycine, the simplest member this molecular family, through in situ measurements in the 67P/Churyumov–Gerasimenko comet (Altwegg et al. 2016), has triggered an intense debate on their chemical origin, with many hypotheses on possible formation pathways, precursors, and intermediates (e.g. Theule et al. 2011; Koch et al. 2008; Woon 2002; Aponte et al. 2017).

Laboratory studies on interstellar ice analogues indicate that amino acids can form via hydration of an aminonitrile compound (H_2N–CHR–CN, Koch et al. 2008), which in turn may be generated under astrophysical conditions in two ways. One pathway, driven by photochemistry, consists in the addition of ammonia to the corresponding nitrile (R–CN, Danger et al. 2011); alternatively, the formation can proceed through the Strecker synthesis, a reaction scheme that has been demonstrated to take place not only in solution, but also in the solid phase (Bossa et al. 2009). This process starts from the condensation of ammonia with an aldehyde (R−CHO, see Rimola et al. 2010) and involves imines (RCH=NH) as reactive intermediates (Walch et al. 2001).

Imines are a class of nitrogen-bearing molecules that have a good record of detection in the ISM. Methanimine (CH_2=NH), the simplest member, was revealed in the ISM in 1973 by Godfrey et al.. Subsequently, other more complex species were identified: ethanimine (CH_3CH=NH, Loomis et al. 2013), *C*-cyanomethanimine (NC−CH=NH, Zaleski et al. 2013; Rivilla et al. 2019), and propargylimine (HC≡C−CH=NH, Bizzocchi et al. 2020). More recently, ketenimine (CH_2=C=NH, Lovas et al. 2006) has been tentatively detected and an upper limit has been reported for propanimine (CH_3CH_2CHNH, Margulès et al. 2022).

Formation routes of imines via tautomerisation (Lovas et al. 2006) or partial hydrogenation on the dust grain surface (Theule et al. 2011; Krim et al. 2019) of nitriles have been put forth in

[1] See also the updated list presented at this URL: http://www.astrochymist.org/astrochymist_ism.html

the past. More recently, a promising hypothesis points to the role of methanimine as the progenitor of complex imines upon the addition or elimination of reactive radicals. Theoretical studies showed that gas-phase reactions of the CN and CCH radicals with CH_2=NH are exothermic and barrierless, leading to *C*-cyanomethanimine (Vazart et al. 2015) and propargylimine (Lupi et al. 2020), respectively. Generalising this idea, we can speculate that more complex members of the same chemical family are produced in the cold ISM through the process Puzzarini (2022)

$$R^{\bullet} + CH_2{=}NH \longrightarrow R{-}CH{=}NH + H^{\bullet}\,, \quad (1)$$

where $R^{\bullet}$ is a generic small radical. Following this scheme, the species allylimine (CH_2=CH−CH=NH, also known as 1-aza-1,3-butadiene) is an interesting candidate for generation through the above reaction with $R^{\bullet}$ being the vinyl radical (CH_2=$CH^{\bullet}$), which is likely to be abundant in the interstellar gas. Many vinyl-containing compounds have been detected so far: CH_2=CHCN, (Gardner & Winnewisser 1975), CH_2=CHOH (Agúndez et al. 2021), CH_2=CHCHO (Hollis et al. 2004), CH_2=$CHNH_2$ Zeng et al. 2021, CH_2=CH−CCH (Cernicharo et al. 2021), and CH_2=CH−C_3N (Kelvin Lee et al. 2021).

To date, allylimine has not been effectively searched for in space as it lacked a satisfactory spectroscopic characterisation. To the best of our knowledge, only two earlier and rather outdated studies are present in the literature. The first laboratory investigation was published by Penn (1978), who recorded the microwave spectra of two structural isomers of this molecule in the 8–26 GHz frequency range using a Stark-modulation spectrometer. A few years later, Brown et al. (1981) investigated a few rotational transitions at centimetre (cm) wavelengths and determined the ^{14}N-quadrupole coupling constants. Both of these studies are based on a very limited data set; the spectroscopic analyses are thus incomplete and lack an accurate treatment of the centrifugal distortion effects.

For the reasons above, we carried out a detailed laboratory investigation of the rotational spectra of the most stable isomers of allylimine extending the frequency coverage well into the millimetre (mm) domain. The goal is to obtain an accurate centrifugal distortion analysis and to generate an improved line catalogue for radio astronomical purposes. Guided by the new laboratory data, we performed a search for allylimine towards the quiescent G+0.693-0.027 molecular clouds (hereafter G+0.693), located at the central molecular zone (CMZ) in the inner ∼500 pc of our Galaxy. In this object, methanimine, cyanomethanimine, and propargylimine have recently been detected (Zeng et al. 2018; Rivilla et al. 2019; Bizzocchi et al. 2020), together with many other molecular species, including several first detections in the ISM (Jiménez-Serra et al. 2020, 2022; Rivilla et al. 2020, 2021b,a, 2022a,b,c; Rodríguez-Almeida et al. 2021a,b; Zeng et al. 2021; Colzi et al. 2022).

The paper is structured as follows. The experimental procedure is described in Sect. 2. A concise account of the molecular properties of allylimine and the theoretical calculations performed to support the data analysis is given in Sect. 3. The spectral analysis is described in Sect. 4, and the astronomical observations in Sect. 5. In Sect. 6 we discuss the results, and in Sect. 7 we draw our conclusions.

2. Experimental details

The rotational spectrum of allylimine has been investigated using two millimetre-wave spectrometers located at the Center for Astrochemical Studies at the Max-Planck-Institut für extraterrestrische Physik in Garching (Germany) and at the Department of Chemistry of the University of Bologna (Italy). In the following we provide a brief description of the two experimental set-ups.

2.1. CASAC spectrometer

The Center for Astrochemical Studies Absorption Cell (CASAC) was employed to record the spectrum of allylimine in the 80–240 GHz range. The instrument has been described comprehensively elsewhere (Bizzocchi et al. 2017) and only a few details relevant for the present study are reported here. The instrument uses an active multiplier chain (Virginia Diodes) as the primary source of millimetre radiation in the 82–125 GHz band. This device is fed by a 9–15 GHz synthesizer locked to a Rb atomic clock for accurate frequency and phase stabilisation. Further multiplier stages, applied in cascade, allow a frequency coverage up to ∼1.1 THz. A closed-cycle He-cooled InSb hot electron bolometer operating at 4 K is used as a detector. The frequency-modulation technique is employed to improve the signal-to-noise ratio (S/N): the source is sine-wave modulated at 50 kHz and the detector output is demodulated at twice this frequency ($2f$ detection) by a lock-in amplifier, so that the second derivative of the actual absorption profile is recorded by the computer-controlled acquisition system.

The same absorption cell and pyrolysis system used to study propargylimine (Bizzocchi et al. 2020) were adopted for this experiment. Allylimine was produced as described by Penn (1978). Diallylamine vapours were flowed through a 1 cm diameter quartz tube heated to 800°C with a typical pressure of 180 mTorr (24 Pa). The pyrolysis products were directly flowed through the absorption cell, which was continuously pumped and kept at a pressure of about 4 mTorr (0.5 Pa).

2.2. Bologna millimetre spectrometer

Rotational spectra between 240 and 310 GHz were recorded using the frequency-modulation millimetre/submillimetre-wave spectrometer located in Bologna (Melosso et al. 2019a,b). A Gunn diode working in the W band (80–115 GHz) coupled to a passive frequency multiplier (WR3.4x3, Virginia Diodes Inc.) was used as the main radiation source, whose frequency is stabilised and controlled through a phase-lock-loop (PLL). A frequency-modulated 75 MHz signal, coming from a centimetre-wave synthesizer (HP8642A), was used as intermediate frequency in the PLL. All the electronics are referenced to a Rb atomic clock. The detection system is composed of a zero-bias detector (WR3.4ZBD, Virginia Diodes Inc.) operating in the 220–330 GHz range and a lock-in amplifier. The latter has the twofold purpose of demodulating the output signal using the $2f$ detection scheme and filtering out some background noise as a resistor-capacitor circuit.

The measurements were performed in a quartz absorption cell surrounded by a 90 cm long tubular oven, using the same set-up recently described by Jiang et al. (2021). The optical elements of the spectrometer were arranged in a double-pass configuration (for further details, see e.g. Melosso et al. 2020a,b) in order to reach an absorption path-length of ∼3 m. Allylimine was produced directly inside the absorption cell by heating diallylamine vapours at a temperature of 500°C. Differently from what was observed in the past for other imines, for which the flash vacuum pyrolysis was performed externally to the absorption cell (Melosso et al. 2018; Melli et al. 2018, 2020), good signals of

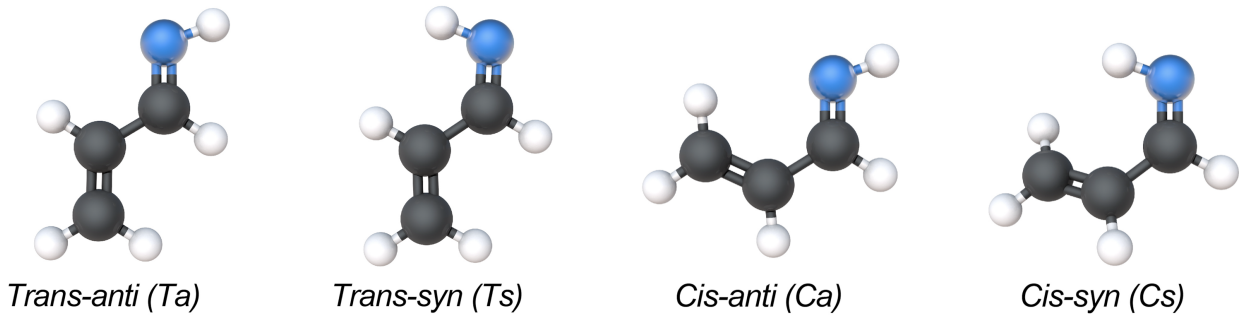

Fig. 1. Isomers of allylamine.

allylimine were already obtained at 100°C. The working temperature of 500°C was chosen with the unique purpose of obtaining stable experimental conditions since the ON/OFF control of the oven causes some oscillation at lower temperatures.

3. Molecular properties

Allylimine can be conveniently illustrated as an iminic moiety –CH=NH connected to a vinyl group CH_2=CH– by a single C–C bond. Depending on the relative orientation of these two subunits, four geometrical isomers can be defined. The prefixes cis- (*C*) and trans- (*T*) are used to identify the position of the two constituents with respect to the central C–C bond, respectively on the same and on the opposite side; the labels syn- (s) and anti- (a) define the position of the iminic H with respect to C=C. The resulting four geometric isomers are depicted in Fig. 1 and are denoted *Ta*, *Ts*, *Ca*, and *Cs*. All forms but *Cs* have a planar structure with C_s symmetry. In the *Cs* form, owing to the repulsion between the iminic H and one terminal vinyl H, the molecular backbone is tilted and the molecular symmetry is C_1, in analogy to trans-butadiene (Baraban et al. 2018) and azabutadiene (Jiang et al. 2022).

The molecular and spectroscopic properties of the four allylimine isomers were evaluated by means of state-of-the-art computational methodologies. Equilibrium structures (and their corresponding energies), which straightforwardly provide equilibrium rotational constants, were computed by exploiting the so-called CCSD(T)/CBS+CV composite scheme (Heckert et al. 2005a,b). This approach is based on the CCSD(T) method (i.e. coupled cluster singles and doubles approximation augmented by a perturbative treatment of triple excitations; Raghavachari et al. 1989) and accounts for the extrapolation to the complete basis set (CBS) limit and core-valence (CV) correlation effects. Vibrational corrections to equilibrium rotational constants, evaluated at a lower level of theory, were incorporated to predict ground-state rotational constants. Quartic and sextic centrifugal distortion parameters as well as first-order molecular properties (dipole moments and nuclear quadrupole coupling constants) were accurately predicted by exploiting CCSD(T) calculations. For nuclear quadrupole coupling constants, vibrational corrections to the equilibrium values were also considered. A detailed account on the quantum-chemical calculations performed is provided in Appendix A.

The relative energies and the electric dipole moments of the four allylimine isomers are reported in Table 1. Our calculations indicate that the *Ta* isomer is the most stable, *Ts* is relatively close at E/k = 403.5 K, while the *Ca* and *Cs* species have higher energies, $E/k > 1400$ K. In the present investigation, we focus on the *Ta* and *Ts* isomers, which are the only two species detected in our laboratory experiments. Both are nearly prolate asymmetric top rotors ($\kappa \sim -0.98$); their dipole moments are rather similar ($|\boldsymbol{\mu}| \approx 2$ D), but they differ in the corresponding principal axis projections. As Table 1 shows, the spectrum of the *Ts* isomer is dominated by *a*-type transitions, whereas the *Ta* species has almost equally strong *a*- and *b*-type spectra.

Table 1. Computed relative energies (CCSD(T)/CBS+CV level of theory) of the four allylimine isomers and their dipole moment components (ae-CCSD(T)/ccpCVQZ level of theory).

Parameter	Unit	*Ta*	*Ts*	*Ca*	*Cs*
E	(cm^{-1})	0.0	282.4	955.2	1200.4
	(K)	0.0	403.49	1364.78	1715.12
μ_a	(D)	1.14	2.44	−0.02	2.40
μ_b	(D)	−1.70	0.79	−1.68	0.44
μ_c	(D)	0.0	0.0	0.0	0.19
$\boldsymbol{\mu}$	(D)	2.05	2.56	1.68	2.44

4. Spectral analysis and results

The rotational spectra of the *Ta* and *Ts* allylimine isomers have been recorded in selected frequency regions from 84 to 307 GHz. Two portions exhibiting typical *a*- and *b*-type patterns are shown in Fig. 2. In line with a nearly prolate rotor and the dipole components of Table 1, the *Ts* spectrum presents strong ${}^aR_{0,1}$ [2] branch transitions spaced by $\Delta\nu \approx (B + C)$. For the *Ta* isomer, instead, ${}^bQ_{1,-1}$ branch band heads spaced by $\Delta\nu \approx 2A - B - C$ dominate the spectrum, leading to a more complicated pattern.

From the computed relative energy (see Table 1), a relative [*Ta*]/[*Ts*] isomer abundance of 3.8 can be estimated at 300 K (4.4×10^{17} at 10 K). From the relative intensity comparison of two closely spaced *Ta* and *Ts* lines recorded under the same experimental conditions (source power, sample pressure, temperature, and modulation depth) we derived [*Ta*]/[*Ts*] = 3.3 ± 0.8,

[2] The symbol ${}^xM_{\delta K_a,\delta K_c}$ is used to identify the transition type of an asymmetric rotor: x stands for the dipole moment component involved; $M = P, Q, R$ for the transitions with $\Delta J = -1, 0, +1$, respectively; δK_a and δK_c for the (signed) change of the K_a and K_c pseudo quantum numbers (Gordy & Cook 1984).

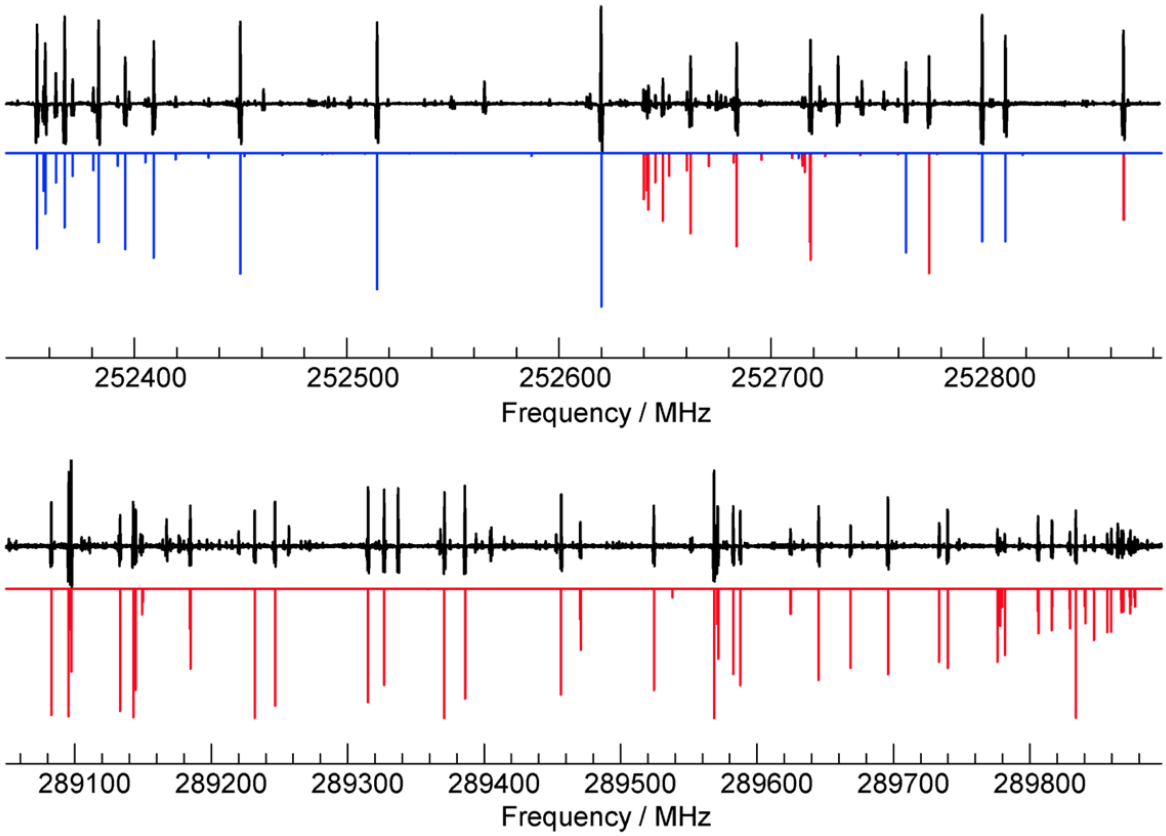

Fig. 2. Portions of the experimental spectrum (in black) showing both *a*- and *b*-type spectral features (blue lines for *Ts*-allylimine and red lines for *Ta*-allylimine). Intensity is in arbitrary units.

in good agreement with the theoretical findings. Therefore, regarding the CASAC experiment, although allylimine is generated at high temperatures, a complete thermalisation is readily achieved in the room temperature absorption cell. On the contrary, the same does not apply to the Bologna experiment, which is characterised by a different set-up.

Owing to the presence of the ^{14}N nucleus with spin $I = 1$ in the molecule, its non-zero nuclear quadrupole moment interacts with the molecular electric field gradient at the nucleus, giving rise to the hyperfine structure of the rotational spectrum. The interaction between the rotational angular momentum $\mathbf{J}$ and the nitrogen nuclear spin $\mathbf{I}_N$ is described by the standard vector coupling scheme:

$$\mathbf{J} + \mathbf{I}_N = \mathbf{F}. \tag{2}$$

As a result, each rotational level with $J > 0$ splits into three hyperfine sub-levels labelled with the total angular quantum number F, where $F = J - 1, J, J + 1$. Therefore, the corresponding transitions are split into several components according to the $\Delta F = 0, \pm 1$ selection rules, with the strongest features having $\Delta F = \Delta J$. An example of these hyperfine patterns is given in Fig. 3.

A total of 617 and 470 lines were recorded for *Ta*- and *Ts*-allylimine, respectively, of which 293 and 65 exhibited resolvable hyperfine features that allowed their components to be assigned. For transitions with unresolved hyperfine structure, the intensity-averaged calculated frequency was instead compared with the recorded line. A few transitions (22 and 10 for *Ta* and *Ts*, respectively) taken from the literature (Penn 1978) were also included in the final data sets. To account for the different measurement precision (σ) of the two experimental sub-sets of data recorded with the CASAC and Bologna spectrometer, distinct statistical weights $w = 1/\sigma^2$ were assigned. The corresponding values are $\sigma = 15$ kHz and $\sigma = 25$–30 kHz (depending on experimental conditions).

The analysis was performed using a Hamiltonian composed of a purely rotational and a hyperfine term:

$$\hat{H} = \hat{H}_{\rm rot} + \hat{H}_{\rm HFS}. \tag{3}$$

Here $\hat{H}_{\rm rot}$ is the S-reduced Watson-type rotational Hamiltonian in its I^r representation (Watson 1977) including the centrifugal distortion up to sextic terms, whereas the hyperfine-structure Hamiltonian $\hat{H}_{\rm HFS}$ describes the ^{14}N-quadrupole interaction making use of the traceless tensor $\boldsymbol{\chi}$, which has χ_{aa} and $\chi_{bb} - \chi_{cc}$ as determinable coefficients. No ^{14}N or H spin-rotation coupling effects were revealed; therefore, the corresponding interaction terms have been neglected in the present analysis.

The spectral analyses were carried out using the `CALPGM` program suite (Pickett 1991). Transitions with the J quantum number as high as 52 and 46 are included for the *Ta* and *Ts* species, respectively, whereas the maximum K_a value reached is 18 and 22, respectively. The spectroscopic constants determined from the fits are collected in Table 2, together with the corresponding computed values. The quality of the fits is expressed by the weighted root mean square $\sigma_{\rm rms}$:

$$\sigma_{\rm rms} = \sqrt{\frac{1}{N}\sum_{i=1}^{N}\left(\frac{x_i^{\rm obs} - x_i^{\rm calc}}{\sigma_i}\right)^2}, \tag{4}$$

where x_i denotes the N data, and σ_i the corresponding assumed uncertainties. For *Ta*- and *Ts*-allylimine, values of 1.03 and

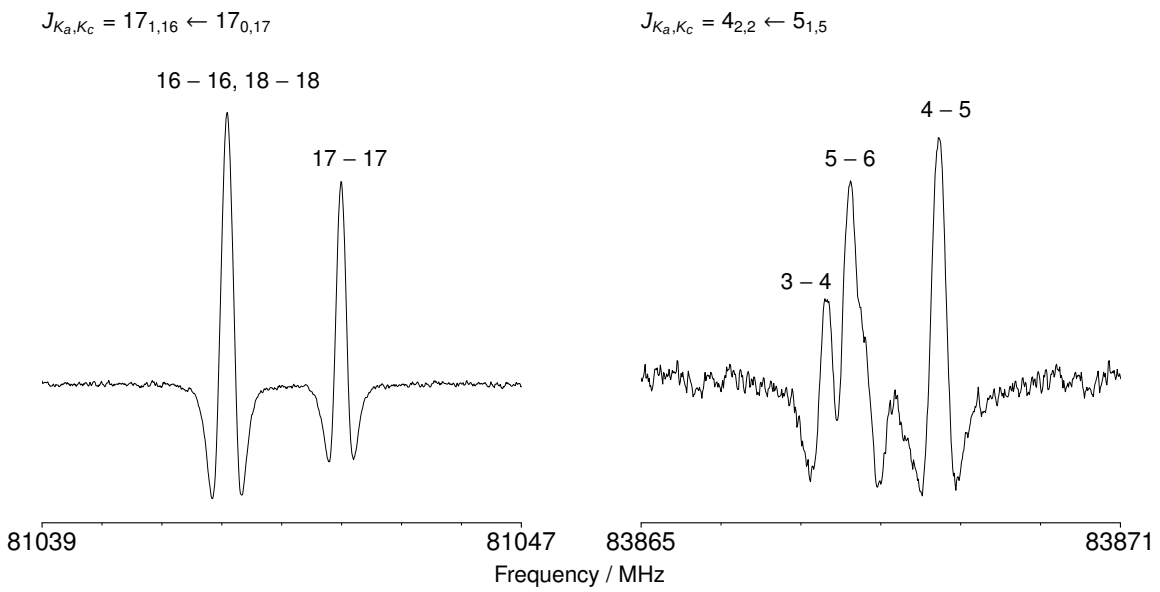

Fig. 3. Recordings of two b-type transitions of *Ta*-allylamine. The nitrogen quadrupole coupling splitting is evident (each hyperfine component has a $F' - F$ label). Left panel: $J_{Ka,Kc}$ $17_{1,16} \leftarrow 17_{0,17}$; right panel: $J_{Ka,Kc} = 4_{2,2} \leftarrow 5_{1,5}$.

Table 2. Spectroscopic constants determined for the *Ta* and *Ts* isomers of allylimine.

		Ta-allylimine		*Ts*-allylimine	
Constant	Unit	Experiment	ab initio[(a)]	Experiment	ab initio[(a)]
A	(MHz)	45773.64504(81)	45797.91440	43755.655(17)	43766.134
B	(MHz)	4560.931313(62)	4561.224130	4564.54014(68)	4565.77443
C	(MHz)	4148.248522(60)	4148.336622	4134.46273(64)	4135.28507
D_J	(kHz)	0.909645(28)	0.9054	0.95037(37)	0.9472
D_{JK}	(kHz)	−7.53100(98)	−7.5174	−7.589(12)	−7.4241
D_K	(kHz)	296.804(27)	286.9488	257.29(74)	243.0085
d_1	(kHz)	−0.107148(13)	−0.1094	−0.114863(46)	−0.1182
d_2	(kHz)	−0.0058627(15)	−0.0055	−0.006237(31)	−0.0059
H_J	(mHz)	0.21719[(b)]	0.21719	0.22243[(b)]	0.22243
H_{JK}	(Hz)	−0.00604(44)	−0.00306	−0.00723(54)	−0.0034
H_{KJ}	(Hz)	−0.2997(20)	−0.3809	−0.196(15)	−0.299
H_K	(Hz)	2.89(24)	4.55	3.61474[(b)]	3.61474
h_1	(mHz)	0.0667(43)	0.0762	0.08093[(b)]	0.08093
h_2	(mHz)	0.01095[(b)]	0.01095	0.01087[(b)]	0.01087
h_3	(mHz)	0.00157[(b)]	0.00157	0.00152[(b)]	0.00152
χ_{aa}	(MHz)	0.751(23)	0.731	−2.963(17)	−2.974
$\chi_{bb} - \chi_{cc}$	(MHz)	−6.985(19)	−6.906	−3.267(10)	−3.263
No. of lines		617		470	
σ_{wrms}		1.03		1.00	
σ_{rms}	(kHz)	103.8		64.2	

Notes. Numbers in parentheses represent 1σ standard deviation in unit of the last digit. [(a)] Equilibrium constants at the CCSD(T)/CBS+CV level, vibrational corrections computed at the fc-CCSD(T)/cc-pVTZ level of theory. Quartic centrifugal distortion constants computed at the CCSD(T)/CBS+CV level. Sextic centrifugal distortion constants computed at the fc-CCSD(T)/pVTZ level of theory. Nuclear quadrupole coupling constants computed at ae-CCSD(T)/cc-pCVQZ level and including vibrational corrections at the ae-MP2/cc-pCVTZ level of theory. See Appendix A for a detailed account. [(b)] Fixed at the computed value.

Table 3. Partition function values and abundance ratios at different temperatures for allylimine isomers.

	Ta-allylimine			*Ts*-allylimine			Isomer ratio
T (K)	$Q_{\rm rot}$	$Q_{\rm HFS}$	$Q_{\rm vib}$	$Q_{\rm rot}$	$Q_{\rm HFS}$	$Q_{\rm vib}$	[*Ta*]/[*Ts*]
2.725	26.410	79.230	1.0000	27.044	93.507	1.0000	6×10^{64}
5.0	64.909	194.726	1.0000	66.470	199.410	1.0000	2×10^{35}
9.375	165.616	496.848	1.0000	169.603	508.809	1.0000	7×10^{18}
18.75	466.788	1400.365	1.0000	478.031	1434.093	1.0000	2×10^{9}
37.5	1318.032	3954.097	1.0000	1349.784	4049.354	1.0001	5×10^{4}
75.0	3725.194	11175.583	1.0436	3814.943	11444.829	1.0577	2×10^{2}
150	10534.861	31604.447	1.3245	10788.605	32365.815	1.3781	15
225	19356.422	58069.266	1.8714	19822.670	59468.011	1.9792	6.1
300	29807.537	89422.612	2.8263	30525.403	91576.209	3.0190	3.8
500	64168.784	192506.343	10.746	65709.506	197128.509	11.606	2.2
1000	180019.528	540056.184	504.77	184077.689	552230.592	546.52	1.5

1.00 were obtained for σ_{rms}, respectively, thus indicating that, on average, the data sets have been reproduced within the experimental uncertainties.

Owing to the new extensive data set, the spectroscopic characterisation of allylimine is considerably improved. Compared to the previous results reported by Penn (1978), the uncertainty of the rotational constants A, B, and C is reduced by three orders of magnitude (a factor of ∼350 for the *Ts* isomer). Additionally, a complete set of quartic centrifugal distortion constants (with a precision of ∼0.1%) plus four sextic terms (two for the *Ts* isomer) are provided for the first time. To give an example of the improvement accomplished, the $J_{Ka,Kc} = 20_{0,20} - 19_{0,19}$ transition, expected to lie at 170.730 GHz with a $\log I$ of –3.82 nm^2 MHz by Penn (1978), is now predicted at 170.726 GHz with a $\log I$ of –3.90 nm^2 MHz, with an offset of 4 MHz between the two sets of data.

The comparison with the computed spectroscopic parameters (also reported in Table 2) points out a very good agreement for the rotational constants, which differ, on average, by only 0.07% from the experimental counterparts. The quartic centrifugal distortion constants, except for the D_{JK} of *Ta*, also compare well with the experimental values, showing an average relative deviation of 3% for the two isomers. It was also possible to constrain the sextic centrifugal distortion constants to a partial set of sextic parameters: H_{JK}, H_{KJ}, H_K, h_1 for the *Ta* isomer and H_{JK}, H_{KJ} for the *Ts* isomer, with the remaining sextic terms kept fixed at the computed values. For the quadrupole coupling constants the agreement is on average within 1.1%.

From the improved spectroscopic constants determined in the present work, two collections of rest frequencies were produced for each isomer, and are accessible at CDMS[3](Müller et al. 2005; Endres et al. 2016); the `<X>allylimine.cat` catalogue list of pure rotational transitions extends up to 300 GHz, whereas the `hfs_<X>allylimine.cat` catalogue is limited to the 3 mm band (ν < 120 GHz), but contains all hyperfine components. The symbol `<X>` in the file names reads as `<Ta->` or `<Ts->` for the corresponding isomers. The catalogues were generated with the `SPCAT` routine (Pickett 1991) and their format matches that of the CDMS and JPL (Pickett et al. 1998) catalogues, thus allowing their straightforward use in astronomic line-analysis tools, such as MADCUBA (Martín et al. 2019), CASSIS (Vastel et al. 2015) and MADEX (Cernicharo, J. 2012).

A selection of rotational ($Q_{\rm rot}$), hyperfine ($Q_{\rm HFS}$), and vibrational ($Q_{\rm vib}$) partition functions for *Ta*- and *Ts*-allylimine is given in Table 3. The values were computed for the 3–1000 K temperature interval and were obtained by direct summation over the rotational or hyperfine levels, whose energies have been accurately determined from the spectral analysis. The vibrational partition functions $Q_{\rm vib}$ were computed using harmonic frequencies at the CCSD(T)/CBS+CV level, which were obtained as explained in Appendix A.

5. Interstellar search towards the G+0.693 molecular cloud

We searched for the *Ta* and *Ts* allylimine isomers towards the G+0.693 molecular cloud, which is located in the SgrB2 N complex of the CMZ of our Galaxy. This region is thought to be affected by a cloud-cloud collision (Zeng et al. 2020) that produced large-scale shocks that sputtered the interstellar dust grains, thus releasing into the gas phase multiple molecules formed on the dust surfaces. This explains the extremely rich chemistry of G+0.693, where many complex organic molecules have been detected.

We exploited a sensitive unbiased spectral survey performed with the Yebes 40 m (Guadalajara, Spain) and the IRAM 30 m (Granada, Spain) telescopes. In both surveys, we used the position switching mode pointed towards α(J2000.0)= $17^{\rm h}47^{\rm m}22^{\rm s}$, δ(J2000.0)= −28°21′27″. We used Yebes 40m observations from 31.075 GHz to 50.424 GHz, and IRAM 30m observations for the 71.770–116.720 GHz, and 124.77–175.5 GHz frequency ranges. More detailed information of the observational survey, including noise levels and spectral resolutions, are available in Rivilla et al. (2021a,b).

We implemented the spectroscopy parameters presented in this work into the MADCUBA package[4]; version 11/03/2022; (Martín et al. 2019). Using the Spectral Line Identification and Modeling (SLIM) tool of MADCUBA, we generated synthetic

[3] https://cdms.astro.uni-koeln.de/cdms/portal/

[4] Madrid Data Cube Analysis on ImageJ is a software developed at the Center of Astrobiology (CAB) in Madrid; http://cab.inta-csic.es/madcuba/

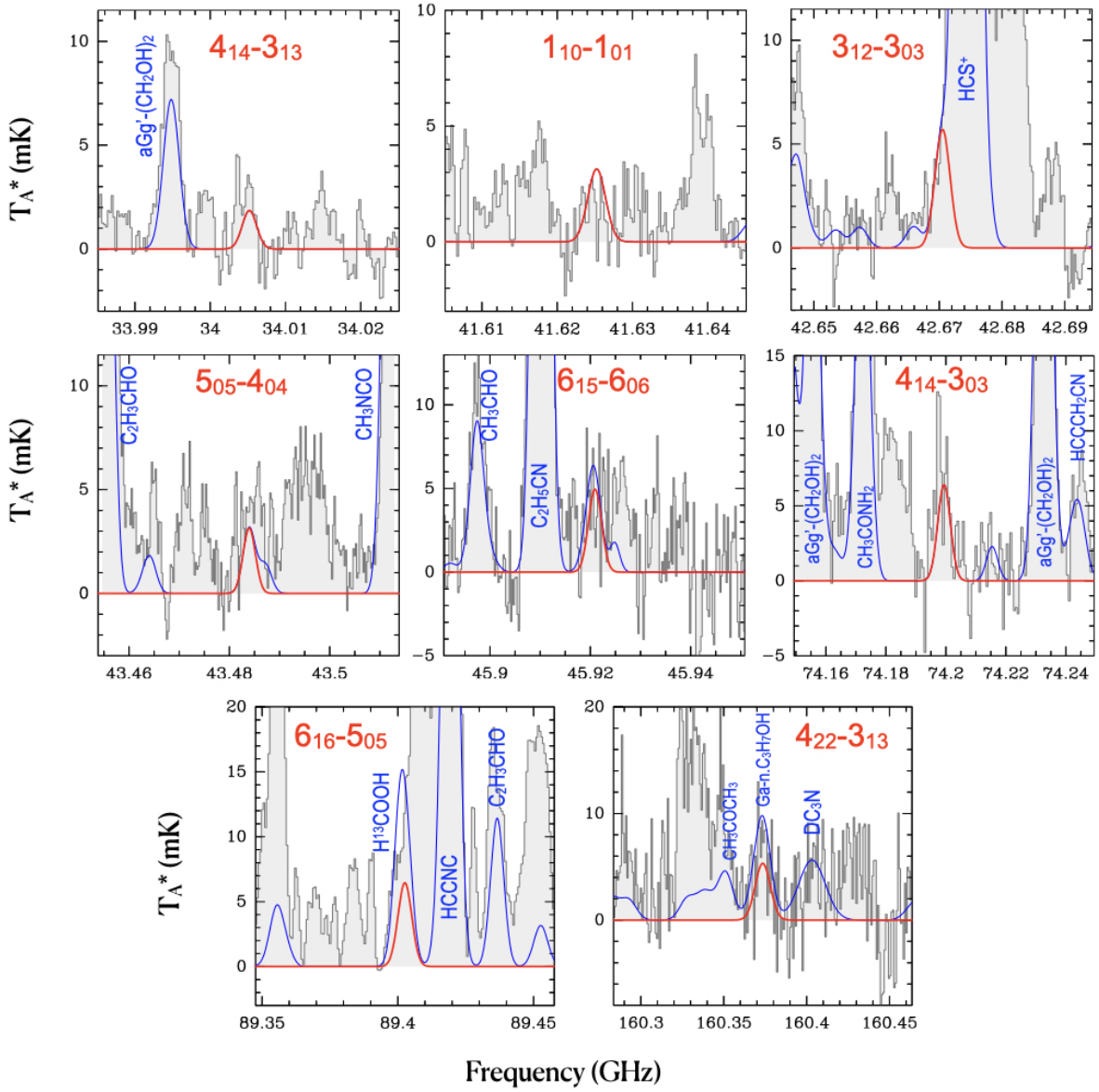

Fig. 4. *Ta*-allylimine transitions tentatively detected towards G+0.693. The observed spectrum is shown in grey histograms. The simulated LTE spectrum of *Ta*-allylimine using the parameters explained in the text (Sect. 5) is indicated by the red curve. The blue curve denotes the contribution of all the species identified in G+0.693, including allylimine. The quantum numbers of the *Ta*-allylimine transitions are provided in each panel.

spectra of the two lowest energy isomers of allylimine (*Ta* and *Ts*) under the assumption of local thermodynamic equilibrium (LTE) to be compared with the observed spectra.

Figure 4 shows the brightest transitions of the *Ta* form that, according to the LTE synthetic spectra, appear unblended or slightly blended with emission from other species already identified in this source, which contributes to reproducing the observed spectra well. The spectroscopic information for these *Ta*-allylimine transitions is shown in Table 4 and in Fig. 4. We note that all the remaining transitions of *Ta*-allylimine predicted within the LTE approximation are heavily contaminated by stronger emission from other species, and that there are no missing lines in the data.

To derive the column density, we used the AUTOFIT tool of SLIM (see Martín et al. 2019), which finds the best fit between the simulated LTE model and the observed spectra. We also considered the contribution to the emission from other molecules. The excitation temperature (T_{ex}) found for most of the molecules detected towards this molecular cloud is low, typically in the range 5–20 K (see e.g. Zeng et al. 2019). This T_{ex} is significantly lower than the kinetic temperature of the cloud (~150K) because the molecules are sub-thermally excited, due to the relatively low density of the cloud (~10^4–10^5 cm^{-3}, Zeng et al. 2020). For this reason, we used the T_{ex} value of 8K derived for a very similar species, propargylimine (Bizzocchi et al. 2020), with a FWHM of 20 km s^{-1} and velocity v_{LSR} = 69 km s^{-1}. We obtained N=(1.5±0.6)×10^{13} cm^{-2}, which implies a molecular abundance compared to molecular hydrogen of ~4×10^{-11}, using $N(H_2)$=1.35×10^{23} cm^{-2} (Martín et al. 2008).

Similarly, several transitions of the *Ts* species are tentatively detected, as shown in Fig. 5 (see Table 4 for their spectroscopic information). In this case, the AUTOFIT algorithm did not converge, so we changed the value of N (leaving the other parameters fixed) until we found a good correspondence with the

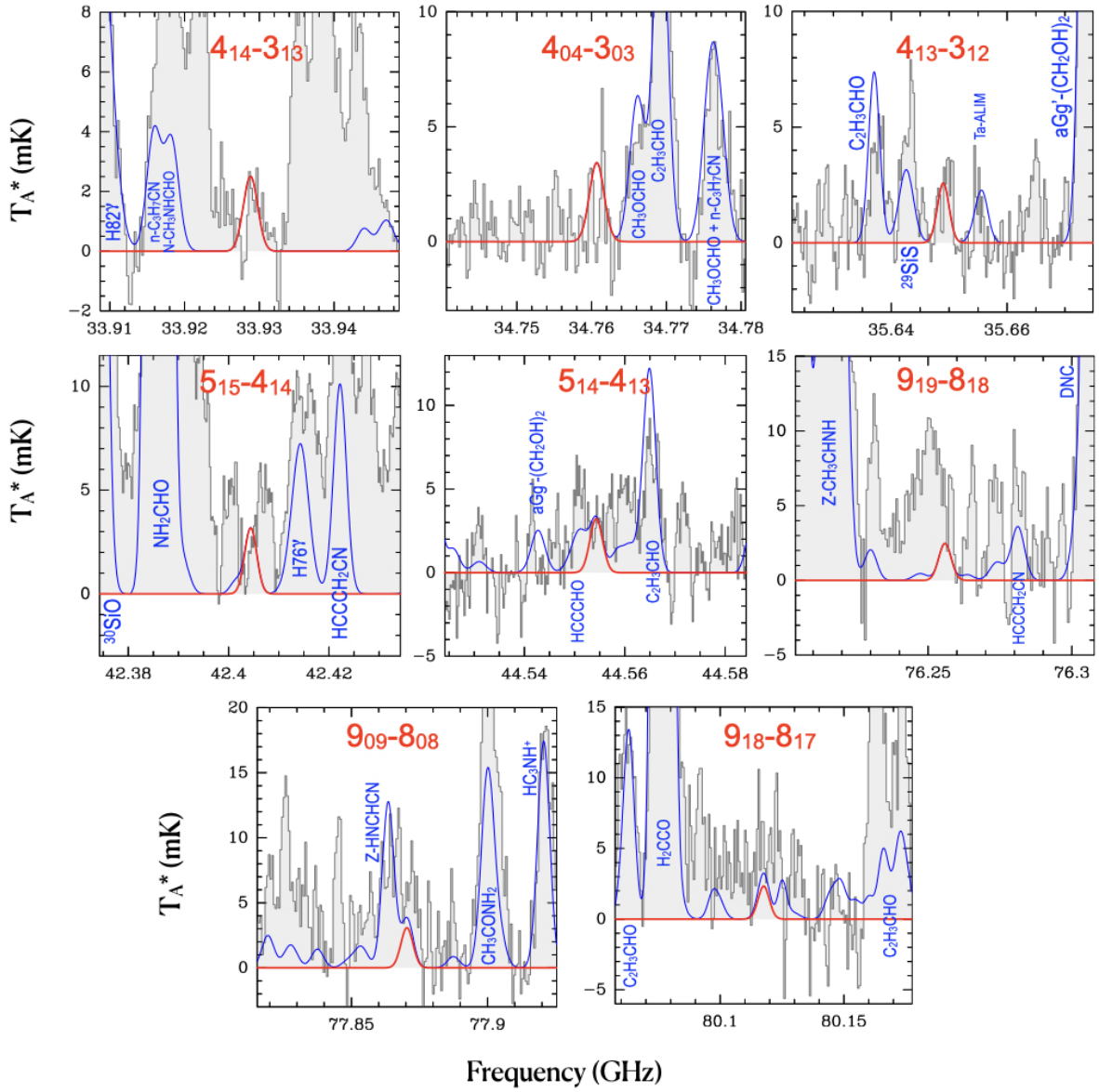

Fig. 5. *Ts*-allylimine transitions tentatively detected towards G+0.693. The observed spectrum is shown in grey histograms. The simulated LTE spectrum of *Ts*-allylimine using the parameters explained in the text (Sect. 5) is indicated by the red curve. The blue curve denotes the contribution of all the species identified in G+0.693, including allylimine. The quantum numbers of the *Ts*-allylimine transitions are indicated in each panel.

observed spectrum. We obtained $N \sim 0.5{\times}10^{13}$ cm^{-2}, a factor of ∼3 less abundant that the *Ta* isomer. This is in good agreement with the results found for other isomers, for which the most stable species is the most abundant, for example cyanomethanimine and propargylimmine (Rivilla et al. 2019; Bizzocchi et al. 2020, respectively).

The tentative detections of both forms of allylimine presented here confirm that these species are less abundant than others imines detected towards G+0.693. The *Ta* isomer is a factor of ∼36, ∼13, and ∼1.6 less abundant than methanimine (CH_2NH, Zeng et al. 2019), Z-cyanomethanimine (Z-HNCHCN, Rivilla et al. 2019), and Z-propargylimine (Z-HCCCHNH, Bizzocchi et al. 2020), respectively. This confirms a clear trend of decreasing molecular abundance with increasing imine complexity, similarly to what is found for other chemical families towards G+0.693, such as alcohols (Jiménez-Serra et al. 2022), isocyanates (Rodríguez-Almeida et al. 2021b), aldehydes (Sanz-Novo et al. 2022), and thiols (Rodríguez-Almeida et al. 2021a).

6. Discussion

The analysis of the transitions tentatively assigned to allylimine in G+0.693 yielded a plausible estimate of its abundance, in line with the trend established by the other detected members of the same class. Starting from methanimine (RCH=NH, with R=H), an inverse relation between the observed abundance and the complexity of the R moiety is highlighted. Recent theoretical investigations on imine formation routes suggest that methanimine may actually act as the main progenitor (Lupi et al. 2020; Puzzarini & Barone 2020), and the processes leading to the various species are substantially influenced by the abundances of the R radicals that take part in the relevant reaction. The column density of allylimine estimated in this work (0.15×10^{14} cm^{-2}, *Ta* isomer) is less than that derived for propargylimine (0.24×10^{14} cm^{-2}, *Z*-isomer, Bizzocchi et al. 2020), thus suggesting a consistent relationship between the CCH and CH_2=CH species. To date, no estimates of the vinyl radical

Table 4. Tentatively observed rotational transitions of both allylimine isomers.

Frequency (GHz)	Transition (J_{K_a,K_c})	log I (nm^2 MHz)	log A_{ul} (s^{-1})	g_u	E_u (K)
		Ta-allylimine			
15034.005084	$4_{1,4}$–$3_{1,3}$	–5.915	–6.61439	9	6.1
41.625114	$1_{1,0}$–$1_{0,1}$	–5.798	–5.93554	3	2.4
42.670365	$3_{1,2}$–$3_{0,3}$	–5.417	–5.91009	7	4.6
43.483824	$5_{0,5}$–$4_{0,4}$	–5.577	–6.25570	11	6.3
45.920789	$6_{1,5}$–$6_{0,6}$	–5.110	–5.82973	13	11.0
74.199397	$4_{1,4}$–$3_{0,3}$	–5.075	–5.43533	9	6.1
89.402598	$6_{1,6}$–$5_{0,5}$	–4.766	–5.19928	13	10.6
160.373509	$4_{2,2}$–$3_{1,3}$	–4.552	–4.57186	9	12.1
		Ts-allylimine			
33.928717	$4_{1,4}$–$3_{1,3}$	–5.277	–5.96658	9	6.0
34.760580	$4_{0,4}$–$3_{0,3}$	–5.225	–5.90658	9	4.2
35.648859	$4_{1,3}$–$3_{1,2}$	–5.234	–5.90309	9	6.2
42.404266	$5_{1,5}$–$4_{1,4}$	–4.978	–5.65561	11	8.0
44.554160	$5_{1,4}$–$4_{1,3}$	–4.936	–5.59007	11	8.3
76.255852	$9_{1,9}$–$8_{1,8}$	–4.218	–4.86012	19	20.2
77.870388	$9_{0,9}$–$8_{0,8}$	–4.192	–4.82681	19	18.7
80.117576	$9_{1,8}$–$8_{1,7}$	–4.176	–4.79588	19	21.1

Notes. Transition frequencies, quantum numbers, base 10 logarithm of the integrated intensity at 300 K (log I), the base 10 logarithm of Einstein coefficients (log A_{ul}), and upper state degeneracy (g_u) are provided.

column density are available, but the abundance ratio of the corresponding cyanides, [HC_3N]/[CH_2=CHCN] ~ 8 (Bizzocchi et al. 2020), points in that direction.

The [E]/[Z] isomeric ratio of imines in the ISM is a topic that has recently attracted some attention (see e.g. Rivilla et al. 2019 and reference therein). Generally speaking, the observed geometrical isomer ratio can be attributed to the combined effects of formation and destruction processes (Vazart et al. 2015; Shingledecker et al. 2020). An alternative hypothesis, which has been recently put forth, suggests that the conversion from the least stable isomer to the most stable one is feasible even at very low temperatures via quantum tunnelling (García de la Concepción et al. 2021). In this framework, the isomeric abundances of imines are governed solely by thermodynamics, and the observed [E]/[Z] ratios should be interpreted in terms of their relative stability. This scenario has had some success in reproducing the isomeric ratios observed in G+0.693 for cyanomethanimine ([Z]/[E] ~ 6), ethanimine ([Z]/[E] = 10–15), and propargylimine ([Z]/[E] > 2), when assuming a kinetic temperature T_{kin} = 150 K. For allylimine, by inserting the energy difference between *Ts* and *Ta* isomers, $\Delta E/k$ = 403.5 K, in Eq. (5) of García de la Concepción et al. (2021), one gets an isomeric ratio [*Ta*/*Ts*] ~ 15, which is higher than the (tentatively) observed value of ~3. This would suggest that there is an extra abundance of the less stable *Ts* isomer with respect to that predicted by thermochemistry. This would also be in contrast relative dipole principle (RDP) proposed by Shingledecker et al. (2020), which postulates an anti-correlation between the relative isomer abundance and the magnitude of their permanent dipole moments (μ_{Ta} = 2.05 D and μ_{Ts} = 2.56 D). Therefore, either the formation of *Ts*-allylimine is kinetically favoured or the two isomers originate from distinct chemical routes.

7. Conclusions

This paper reports on an extensive spectroscopic characterisation of allyllimine, CH_2=CH–CH=NH, a species that represents a higher level of complexity compared to the previous members of the same chemical class already detected in the ISM. Measurements have been performed between 84 and 300 GHz, with the recording of 617 and 470 new rotational transitions for the two most stable *Ta* and *Ts* isomers, respectively. The resulting data sets were analysed using an S-reduced rotational Hamiltonian, yielding a very precise set of rotational constants, a full set of quartic coefficients, and some sextic centrifugal distortion coefficients. A number of lines showed resolvable hyperfine structure due to the quadrupole interaction of the ^{14}N nucleus with molecular rotation. For these transitions, each hyperfine component was accurately measured and analysed to determine the corresponding coupling coefficients. High-level theoretical calculations were performed to assist the spectral assignment and the analysis of the laboratory data. In particular, ab initio values were used as suitable constraints for the Hamiltonian coefficients which could not be adjusted in the least-squares fit. Overall, the agreement between experimentally derived constants and the corresponding theoretical prediction is very good.

The new extensive set of spectroscopic parameters (see Table 2) was employed to generate catalogues of highly precise rest frequencies for the *Ta* and *Ts* isomers at millimetre wavelengths. These data were used to perform a search for allylimine emission lines in a spectral survey of the molecular cloud G+0.693 located in the CMZ. Eight transitions for each isomers have been tentatively assigned, leading to the derivation of the column densities $N = (1.5 \pm 0.6) \times 10^{13}$ cm^{-2} for *Ta* and $N \sim 0.5 \times 10^{13}$ cm^{-2} for *Ts*. These values are lower than those of the simpler related species cyanomethanimine and propargylimine, in agreement with the expected trend. The resulting [*Ta*]/[*Ts*] isomer ratio is ~3, much lower than the value of ~15 that can be estimated on the basis of thermodynamic considerations.

Acknowledgements. We thank the Max Planck society for the financial support. The work at Bologna University was supported by RFO funds and MIUR (PRIN Grant Number 202082CE3T). We are grateful to the IRAM 30 m and Yebes 40 m telescope staff for help during the different observing runs. IRAM is supported by the National Institute for Universe Sciences and Astronomy/National Center for Scientific Research (France), Max Planck Society for the Advancement of Science (Germany), and the National Geographic Institute (IGN) (Spain). The 40m radio telescope at Yebes Observatory is operated by the IGN, Ministerio de Transportes, Movilidad y Agenda Urbana. V.M.R. has received support from the Comunidad de Madrid through the Atracción de Talento Investigador Modalidad 1 (Doctores con experiencia) Grant (COOL:Cosmic Origins of Life; 2019-T1/TIC-5379), and the Ayuda RYC2020-029387-I funded by MCIN/AEI /10.13039/501100011033. A.P.C. gratefully acknowledges the super-computing facilities of CINECA (project "CINEMA", grant HP10C2QE6F) and SCSCF ("Sistema per il Calcolo Scientifico di Ca' Foscari", a multiprocessor cluster system owned by Università Ca' Foscari Venezia).

References

Agúndez, M., Marcelino, N., Tercero, B., et al. 2021, A&A, 649, A4
Altwegg, K., Balsiger, H., Bar-Nun, A., et al. 2016, Sci. Adv., 2, e1600285
Aponte, J. C., Elsila, J. E., Glavin, D. P., et al. 2017, ACS Earth Space Chem., 1, 3
Aponte, J. C., Elsila, J. E., Hein, J. E., & Dworkin, J. P. 2020, Meteor. Planet. Sci., 55, 2422
Baraban, J., Martin-Drumel, M. A., Changala, P. B., et al. 2018, Angew. Chem. Int. Ed., 57, 1821
Bizzocchi, L., Lattanzi, V., Laas, J., et al. 2017, A&A, 602, A34
Bizzocchi, L., Prudenzano, D., Rivilla, V. M., et al. 2020, A&A, 640, A98
Bossa, J. B., Theule, P., Duvernay, F., & Chiavassa, T. 2009, ApJ, 707, 1524
Brown, R. D., Godfrey, P. D., & Winkler, D. A. 1981, Chem. Phys., 59, 243

Cernicharo, J. 2012, EAS Publ. Ser., 58, 251
Cernicharo, J., Agúndez, M., & Cabezas. 2021, A&A, 647, A2
Colzi, L., Martín-Pintado, J., Rivilla, V. M., et al. 2022, ApJ, 926, L22
Danger, G., Bossa, J.-B., de Marcellus, P., et al. 2011, A&A, 525, A30
Endres, C. P., Schlemmer, S., Schilke, P., Stutzki, J., & Müller, H. S. P. 2016, J. Mol. Spectrosc., 327, 95
Feller, D. 1992, J. Chem. Phys., 96, 8
Frisch, M. J., Trucks, G. W., Schlegel, H. B., et al. 2016, Gaussian 16 Revision C.01 (Wallingford, CT: Gaussian Inc.)
García de la Concepción, J., Jiménez-Serra, I., Carlos Corchado, J., Rivilla, V. M., & Martín-Pintado, J. 2021, ApJ, 912, L6
Gardner, F. F., & Winnewisser, G. 1975, ApJ, 195, L127
Godfrey, P. D., Brown, R. D., Robinson, B. J., & Sinclair, M. W. 1973, ApJL, 13, 119
Gordy, W., & Cook, R. L. 1984, Microwave Molecular Spectra, 3rd edn. (Wiley New York), 929
Heckert, M., Kállay, M., & Gauss, J. 2005a, Mol. Phys., 103, 2109
Heckert, M., Kállay, M., Tew, D. P., Klopper, W., & Gauss, J. 2005b, J. Chem. Phys., 125, 044108
Helgaker, T., Klopper, W., Koch, H., & Noga, J. 1997, J. Chem. Phys., 106, 9639
Herbst, E., & van Dishoeck, E. F. 2009, ARA&A, 47, 427
Hollis, J. M., Jewell, P. R., Lovas, F. J., Remijan, A., & Møllendal, H. 2004, ApJ, 610, L21
Jiang, N., Melosso, M., Tamassia, F., et al. 2021, Front. Astron. Space Sci., 8, 29
Jiang, N., Melosso, M., Bizzocchi, L., et al. 2022, J. Phys. Chem. A, 126, 1881
Jiménez-Serra, I., Martín-Pintado, J., Rivilla, V. M., et al. 2020, Astrobiology, 20, 1048
Jiménez-Serra, I., Rodriguez-Almeida, L. F., Martin-Pintado, J., et al. 2022, A&A 663, A181
Kelvin Lee, K. L., Loomis, R. A., Burkhardt, A. M., et al. 2021, ApJL, 908, L11
Koch, D. M., Toubin, C., Peslherbe, G. H., & Hynes, J. T. 2008, J. Phys. Chem. C, 112, 2972
Krim, L., Guillemin, J.-C., & Woon, D. E. 2019, MNRAS, 485, 5210
Loomis, R. A., Zaleski, D. P., Steber, A. L., et al. 2013, ApJ, 765, L9
Lovas, F. J., Hollis, J. M., Remijan, A. J., & Jewell, P. R. 2006, ApJ, 645, L137
Lupi, J., Puzzarini, C., & Barone, V. 2020, ApJ, 903, L35
Margulès, L., Remijan, A., Belloche, A., et al. 2022, A&A, 663, A132
Martín, S., Requena-Torres, M. A., Martín-Pintado, J., & Mauersberger, R. 2008, ApJ, 678, 245
Martín, S., Martín-Pintado, J., Blanco-Sánchez, C., et al. 2019, A&A, 631, A159
Matthews, D. A., Cheng, L., Harding, M. E., et al. 2020, J. Chem. Phys., 152, 214108
Melli, A., Melosso, M., Tasinato, N., et al. 2018, ApJ, 855, 123
Melosso, M., Melli, A., Puzzarini, C., et al. 2018, A&A, 609, A121
Melosso, M., Bizzocchi, L., Tamassia, F., et al. 2019a, Phys. Chem. Chem. Phys., 21, 3564
Melosso, M., Conversazioni, B., Degli Esposti, C., et al. 2019b, JQSRT, 222, 186
Melli, A., Potenti, S., Melosso, M., et al. 2020, Chem. Eur. J., 26, 15016
Melosso, M., Achilli, A., Tamassia, F., et al. 2020a, JQSRT, 248, 106982
Melosso, M., Dore, L., Gauss, J., & Puzzarini, C. 2020b, J. Mol. Spectrosc., 111291
Mills, I. 1972, in Molecular Spectroscopy: Modern Research, eds. K. N. Rao, & C. W. Matthews (Academic Press), 115
Møller, C., & Plesset, M. S. 1934, Phys. Rev., 46, 618
Müller, H. S. P., Schlöder, F., Stutzki, J., & Winnewisser, G. 2005, J. Mol. Struct., 742, 215
Penn, R. E. 1978, J. Mol. Spectrosc., 69, 373
Pickett, H. M. 1991, J. Mol. Spectrosc., 148, 371
Pickett, H. M., Poynter, R. L., Cohen, E. A., et al. 1998, J. Quant. Spec. Radiat. Transf., 60, 883
Pietropolli Charmet, A., & Cornaton, Y. 2018, J. Mol. Struct., 1160, 455
Puzzarini, C. 2022, Front. Astron. Space Sci., 8, 811342
Puzzarini, C., & Barone, V. 2020, Phys. Chem. Chem. Phys., 22, 6507
Puzzarini, C., Cazzoli, G., Harding, M. E., Vázquez, J., & Gauss, J. 2009, J. Chem. Phys., 131, 234304
Puzzarini, C., Stanton, J. F., & Gauss, J. 2010, Int. Rev. Phys. Chem., 29, 273
Raghavachari, K., Trucks, G. W., Pople, J. A., & Head-Gordon, M. 1989, CPL, 157, 479
Rimola, A., Sodupe, M., & Ugliengo, P. 2010, Phys. Chem. Chem. Phys., 12, 5285
Rivilla, V., Martín-Pintado, J., Jiménez-Serra, I., et al. 2019, MNRAS Lett., 483, L114
Rivilla, V. M., Martín-Pintado, J., Jiménez-Serra, I., et al. 2020, ApJ, 899, L28
Rivilla, V. M., Jiménez-Serra, I., Martín-Pintado, J., et al. 2021a, Proc. Natl. Acad. Sci. U.S.A., 118, 2101314118
Rivilla, V. M., Jiménez-Serra, I., García de la Concepción, J., et al. 2021b, MNRAS, 506, L79
Rivilla, V. M., Colzi, L., Jiménez-Serra, I., et al. 2022a, ApJ, 929, L11
Rivilla, V. M., García De La Concepción, J., Jiménez-Serra, I., et al. 2022b, Front. Astron. Space Sci., 9, 829288
Rivilla, V. M., Jiménez-Serra, I., Martín-Pintado, J., et al. 2022c, Front. Astron. Space Sci., 9, 876870
Rodríguez-Almeida, L. F., Jiménez-Serra, I., Rivilla, V. M., et al. 2021a, ApJ, 912, L11
Rodríguez-Almeida, L. F., Rivilla, V. M., Jiménez-Serra, I., et al. 2021b, A&A, 654, L1
Sanz-Novo, M., Belloche, A., Rivilla, V. M., et al. 2022, A&A 666, A114
Shingledecker, C. N., Molpeceres, G., Rivilla, V. M., Majumdar, L., & Kästner, J. 2020, ApJ, 897, 158
Snyder, L. E., Lovas, F. J., Hollis, J. M., et al. 2005, ApJ, 619, 914
Theule, P., Borget, F., Mispelaer, F., et al. 2011, A&A, 534, A64
Vastel, C., Bottinelli, S., Caux, E., et al. 2015, SF2A-2015: Proceedings of the Annual meeting of the French Society of Astronomy and Astrophysics
Vazart, F., Latouche, C., Skouteris, D., Balucani, N., & Barone, V. 2015, ApJ, 810, 111
Walch, S. P., Bauschlicher, C. W., Ricca, A., & Bakes, E. L. O. 2001, Chem. Phys. Lett., 333, 1524
Watson, J. K. G. 1977, in Vibrational Spectra and Structure, ed. J. Durig, (Amsterdam: Elsevier), 6, 1
Woon, D. E. 2002, ApJ, 571, L177
Woon, D. E., & Dunning, Thom H., J. 1995, J. Chem. Phys., 103, 4572
Zaleski, D. P., Seifert, N. A., Steber, A. L., et al. 2013, ApJ, 765, L10
Zeng, S., Jiménez-Serra, I., Rivilla, V. M., et al. 2018, MNRAS, 478, 2962
Zeng, S., Quénard, D., Jiménez-Serra, I., et al. 2019, MNRAS, 484, L43
Zeng, S., Zhang, Q., Jiménez-Serra, I., et al. 2020, MNRAS, 497, 4896
Zeng, S., Jiménez-Serra, I., Rivilla, V. M., et al. 2021, ApJ, 920, L27

Appendix A: Details of the theoretical calculations

As mentioned in the main text, equilibrium geometries (and the corresponding energies) were evaluated using the CCSD(T)/CBS+CV composite scheme. The extrapolation to the CBS limit was performed considering Hartree-Fock Self Consistent Field (HF-SCF) and CCSD(T) correlation energy separately. For HF-SCF, the three-point exponential extrapolation formula by Feller (1992) was used in conjunction with the cc-pVnZ basis sets, with n=T,Q,5. For CCSD(T), the n^{-3} formula by Helgaker et al. (1997) and the cc-pVTZ and cc-pVQZ basis sets were employed. The CV contribution was computed as the difference between the all-electron (ae) computation and the corresponding frozen-core (fc) computation at the CCSD(T)/cc-pCVTZ level (Woon & Dunning 1995). Equilibrium geometries straightforwardly provided equilibrium rotational constants that were corrected for vibrational effects. The corresponding corrections were determined within vibrational perturbation theory to second order (VPT2) (Mills 1972) and required anharmonic force field calculations, which were performed at the fc-CCSD(T)/cc-pVTZ level. These computations also provided, as a by-product, sextic centrifugal distortion constants. The CCSD(T)/CBS+CV composite scheme has also been employed for harmonic force field calculations, which led to the determination of the harmonic vibrational frequencies collected in Table A.1 and, as a by-product, the quartic centrifugal distortion constants. Nuclear quadrupole coupling constants were computed at the CCSD(T)/cc-pCVQZ level correlating all electrons because, as is well known from the literature (Puzzarini et al. 2010), they require a basis set of at least quadruple-zeta quality and the correlation of core electrons. Furthermore, for quantitative predictions, vibrational corrections need to be incorporated (Puzzarini et al. 2009), that were evaluated using second-order Møller-Plesset perturbation theory (MP2; Møller & Plesset (1934)) in conjunction with the cc-pCVTZ basis set. The CFOUR quantum chemistry package (Matthews et al. 2020) was employed for all CCSD(T) calculations, while the Gaussian16 software (Frisch et al. 2016) was used for MP2 computations. Sextic centrifugal distortion constants were obtained with an in-house program (Pietropolli Charmet & Cornaton 2018).

Table A.1. Harmonic vibrational frequencies.

Mode	Symm.	*Ta*	*Ts*
ν_1	A'	3486.3	3436.9
ν_2	A'	3250.8	3252.2
ν_3	A'	3193.1	3165.6
ν_4	A'	3154.6	3154.2
ν_5	A'	3052.3	3108.4
ν_6	A'	1702.4	1697.9
ν_7	A'	1643.8	1640.3
ν_8	A'	1455.8	1454.6
ν_9	A'	1401.3	1409.6
ν_{10}	A'	1304.4	1312.3
ν_{11}	A'	1273.1	1278.6
ν_{12}	A'	1111.3	1124.6
ν_{13}	A'	925.8	925.8
ν_{14}	A'	558.9	551.7
ν_{15}	A'	314.1	311.1
ν_{16}	A''	1105.4	1127.9
ν_{17}	A''	1018.5	1005.3
ν_{18}	A''	953.5	957.4
ν_{19}	A''	856.1	869.8
ν_{20}	A''	579.7	575.6
ν_{21}	A''	168.5	154.0

Notes. Best-estimate values of the harmonic frequencies obtained at the CCSD(T)/CBS+CV level of theory. Reported values are in cm^{-1}.